Amplitude preserving migration through regularized linearized waveform inversion

Ettore Biondi, Mark A. Meadows, and Biondo Biondi

ABSTRACT

Preserving the elastic amplitude behavior of the recorded primary reflections is necessary to perform any amplitude-versus-offset (AVO) analysis within a prestack image space. We show how the extended subsurface-offset image space is able to preserve the elastic behavior of the primary reflections even when these events are acoustically migrated using a reverse-time-migration (RTM) approach performed in a least-squares fashion. On a single interface model, we show that the amplitude of the angle-domain-transformed subsurface-offset image closely follows the theoretical Zoeppritz response even at critical angle. In addition, on a multi-layer model we demonstrate how a regularization term can improve the coherency of the amplitude across different reflection angles when coarse shot sampling causes uneven illumination.

INTRODUCTION

The extended-image space domain has been employed by many authors to invert for the subsurface migration velocity based on optimal focusing of the image when the correct velocity is used during migration (Symes and Kern, 1994; Biondi and Sava, 1999; Shen, 2005; Symes, 2008; Yang and Sava, 2009; Biondi and Almomin, 2014). In other applications a form of extended-image space based on ray parameter is used to generate angle gathers that preserve the amplitude information of the migrated events (Prucha and Biondi, 2002; Kuehl and Sacchi, 2002; Wang et al., 2005). The ability to preserve the amplitude behavior of primary reflected events allows for the analysis of the amplitude-versus-angle (AVA) information and its subsequent inversion to retrieve the elastic subsurface parameters (Schleicher et al., 1993; Albertin et al., 2004; Zhang et al., 2004; Gray and Bleistein, 2009).

In this work we employ acoustic wave-equation migration operators to migrate elastic pressure waves. We make use of the extended subsurface-offset space in order to preserve all the recorded energy present in the shot records (Symes, 2008). Migration is performed by solving a least-squares inverse problem in which we add a regularization term to improve the focusing of the offset-domain common-image gathers (ODCIGs), which in turn results in higher coherency of the angle-domain common-image gathers (ADCIGs). In fact, Prucha and Biondi (2002) demonstrate the ability of a regularized approach to increase the coherency of the image in subsalt

sections. To transform the ODCIGs into ADCIGs we follow the approach proposed by Sava and Fomel (2003), in which we make the transformation unitary, as shown by Biondi (2003).

In two synthetic examples we quantitatively demonstrate how the energy of elastic primary reflected events is mapped into the angle domain. In the first (single-layer) example, we show how the amplitudes of the ADCIGs closely follow, up to a constant factor, the angle-dependent plane-wave reflection coefficients predicted by the Zoeppritz equation even up to and beyond critical incidence angle (Aki and Richards, 2002). In the second test, we employ a layered earth model in which different AVO classes are considered. In this case, we show how a regularization term increases the coherence of the ADCIGs along the angle axis, in addition to producing images in which the amplitude is proportional to the Zoeppritz reflection coefficients.

THEORY

The imaging of primary reflected energy can be posed as an inverse problem by minimizing the following objective function:

$$\phi(\tilde{\mathbf{m}}) = \frac{1}{2}\left\|\tilde{\mathbf{B}}\tilde{\mathbf{m}} - \mathbf{d}\right\|_2^2, \tag{1}$$

where $\mathbf{B}$ represents the extended acoustic wave-equation Born operator, $\tilde{\mathbf{m}}$ is the extended subsurface-offset image, and $\mathbf{d}$ is the recorded data. The goal is to find an optimal extended image $\tilde{\mathbf{m}}$ that matches the amplitudes of the recorded data in a least-squares sense. In order to map the extended image into the data space the following scattering condition is applied:

$$r(\mathbf{x},t) = \int s(\mathbf{x}-2\mathbf{h},t)\tilde{m}(\mathbf{x}-\mathbf{h},\mathbf{h})d\mathbf{h}, \tag{2}$$

where $\tilde{m}$ is the continuous representation of $\tilde{\mathbf{m}}$, $\mathbf{x}$ and $\mathbf{h}$ are the subsurface position and offset, respectively, r is the scattered wavefield, and s the source wavefield, which is the solution of the following partial-differential equation:

$$\left[\frac{\partial^2}{\partial t^2} - v^2(\mathbf{x})\nabla^2\right] s(\mathbf{x},t) = f(\mathbf{x},t), \tag{3}$$

where $v(\mathbf{x})$ is the migration velocity used during the minimization of equation 1 and $f(\mathbf{x},t)$ represents the forcing term. Once the scattered wavefield r is found, it is then used in equation 3 as a forcing term and is propagated through the subsurface. Finally, we extract data at the receiver locations. During the adjoint process (i.e., $\mathbf{B}^*$), the adjoint wavefield r^* is combined with the source wavefield s to produce an extended image $\tilde{m}$ through the following imaging condition:

$$\tilde{m}(\mathbf{x},\mathbf{h}) = \int s(\mathbf{x}-\mathbf{h},t)r^*(\mathbf{x}+\mathbf{h},t)dt. \tag{4}$$

The adjoint wavefield r^* is obtained by solving the adjoint wave equation in which the residuals arising during the inversion are injected as a forcing term. In order to improve the inversion results, a regularization term can be added to equation 1, so that the objective function to minimize becomes the following:

$$\phi_{REG_\gamma}(\tilde{\mathbf{m}}) = \frac{1}{2}\left\|\tilde{\mathbf{B}}\tilde{\mathbf{m}} - \mathbf{d}\right\|_2^2 + \frac{\epsilon^2}{2}\left\|\mathbf{D}_\gamma R_\gamma \tilde{\mathbf{m}}\right\|_2^2, \tag{5}$$

where $\mathbf{D}_\gamma$ represents the regularization operator that enhances the undesired features (which will be diminished during the inversion) in the image $\tilde{\mathbf{m}}$, R_γ is the subsurface offset-to-angle transform, and ϵ is a scalar weight associated with the regularization term. The operator $\mathbf{D}_\gamma$ is a derivative along the angle axis. As shown in the appendix and by Shen (2005), the inverse problem of equation 5 is equivalent to minimizing the following objective function:

$$\phi_{REG_h}(\tilde{\mathbf{m}}) = \frac{1}{2}\left\|\tilde{\mathbf{B}}\tilde{\mathbf{m}} - \mathbf{d}\right\|_2^2 + \frac{\epsilon^2}{2}\left\|\mathbf{D}\tilde{\mathbf{m}}\right\|_2^2, \tag{6}$$

where $\mathbf{D}$ represents the differential semblance operator (DSO) (Symes and Carazzone, 1991). By adding this regularization operator we seek to increase the focusing of the image at zero subsurface offset, which, in turn, enhances coherency across angles once the ODCIGs are transformed into ADCIGs (equation 5). Once the solution of either of the optimization problems expressed in equation 1 or 6 is found, we transform the extended image from subsurface offset to reflection angle, as shown by Biondi (2003):

$$\tilde{m}(\mathbf{x},\mathbf{h}) \xRightarrow[\text{slant stack}]{\text{unitary}} \tilde{m}(\mathbf{x},\gamma). \tag{7}$$

NUMERICAL EXAMPLES

In this section we show where the energy of the recorded data is mapped into the extended-image space after the inverse problems introduced in the previous section are solved iteratively using a linear conjugate-gradient (CG) approach (Aster et al., 2005). The iteration process is necessary to fully map the amplitude of the reflected events into the extended-image space. In both examples we employ an explosive source with energy between 2 and 30 Hz and a flat spectrum between 5 and 24 Hz, which is propagated through an elastic isotropic medium and recorded at the surface as the pressure-wave component of the elastic wavefield. In addition, before migrating the data we remove the direct arrival by modeling it using the properties of the first layer. Furthermore, we extend the image only in the horizontal subsurface-offset domain.

The elastic parameter profiles of the first example are shown in Figure 1. In this case, all three elastic parameters increase across the single interface. We propagate 141 sources and record the pressure component of the elastic wavefield with 351 receivers placed at the surface with spacing of 25 and 10 meters, respectively. A representative shot gather is shown in Figure 2, in which a clear polarity inversion

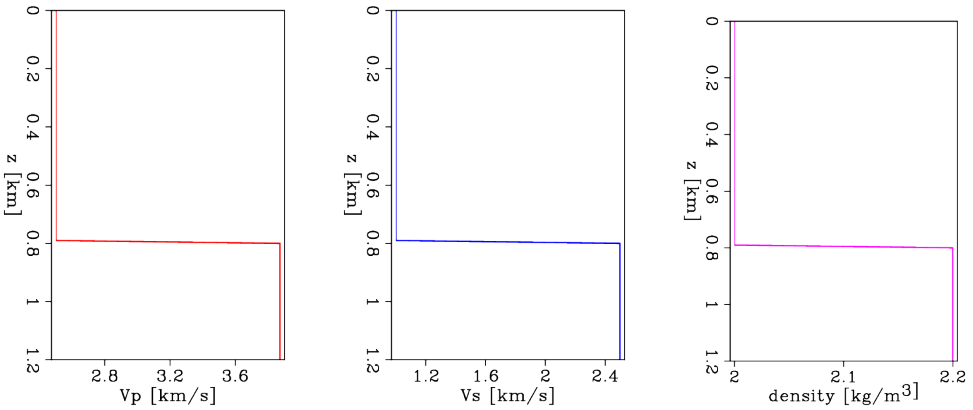

Figure 1: Elastic parameter profiles of the first example. [**ER**]

can be observed. In addition, a weak refracted event is recorded at offsets greater than 2 km. We then minimize equation 1 by applying 200 iterations of a CG method which results in a close match of the recorded elastic amplitudes (Figure 3), meaning that the energy of the elastic pressure is almost entirely mapped into the extended domain. We use the compressional-wave velocity of the first layer for the migration velocity (i.e., the correct migration velocity). The optimal ODCIG for $x = 1.7$ km is shown in Figure 4a, whereas Figure 4b displays the ADCIG at the same x location. Since we used the correct migration velocity, the reflected event focuses at zero subsurface offset. In addition, given the acquisition geometry, the maximum recorded reflection angle is approximately 63°; this offset limitation is clearly visible in the ADCIG where little energy at high angles is present. Finally, the energy of the head wave, recorded at the farthest offsets, is mapped as a linear event in the ODCIG. On the other hand, in the ADCIG, this event is mapped along trajectories following a tangent function behavior.

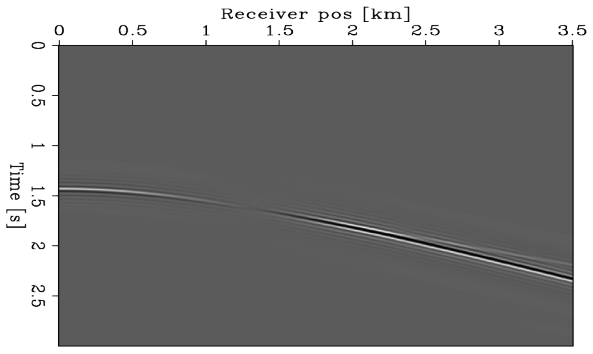

Figure 2: Representative shot gather for the single-interface model in which the explosive source is placed at the origin. In this gather, the direct arrival has been removed. [**ER**]

To quantitatively demonstrate the ability of the extended-image space to preserve the AVA elastic behavior of the recorded waves, we compare the amplitude of the ADCIG extracted at the interface depth (i.e., $z = 0.8$ km) with the computed reflection coefficient using the Zoeppritz equation (Figure 5). We scaled the amplitude of the image so that the zero-angle responses of the two curves are equal. From this

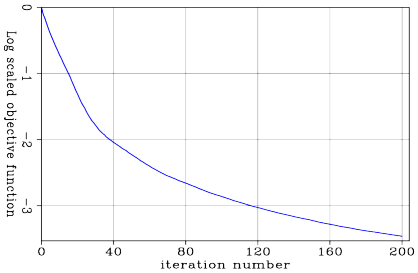

Figure 3: Convergence curve of the iterative least-squares migration process for the single-interface model. [**CR**]

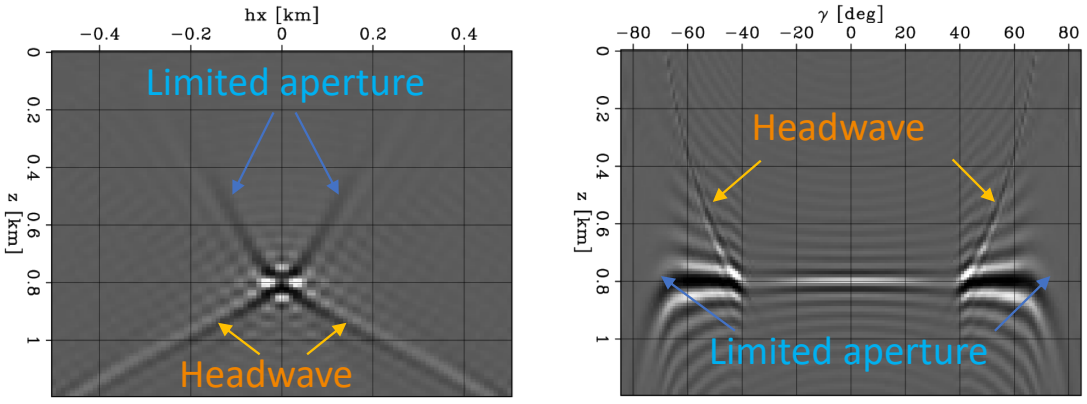

(a) (b)

Figure 4: Extended-space common image gather for $x = 1.7$ km. Left: ODCIG. Right: ADCIG. In both panels the arrows indicate how the energy of recorded events is mapped into the extended-image space. [**CR**]

figure we clearly see that the amplitude-vs-angle response of the image closely follows the one predicted by the Zoeppritz equation, even at and beyond the critical angle of 40°. The mismatch after the critical angle is due to the truncation of the iterative inversion process. To highlight the importance of using an extended-domain image, we compare the elastic plane-wave Zoeppritz reflection coefficient against the acoustic one (blue curves in Figure 6). From this Figure we can clearly see that the acoustic response is completely different than the elastic one, meaning that a non-extended acoustic migration certainly could not capture the elastic amplitude behavior. In addition, in the same Figure we display the point-source responses for the two cases (red curves). These responses are obtained by extracting the amplitudes of the reflected event along the correct traveltime curve within a common-shot gather such as the one of Figure 2. In both cases, the plane-wave and point-source responses start diverging as the angle of incidence increases. This observation underscores the importance of performing any AVA analysis for high angles within ADCIGs, which are able to correctly match the elastic plane-wave Zoeppritz response.

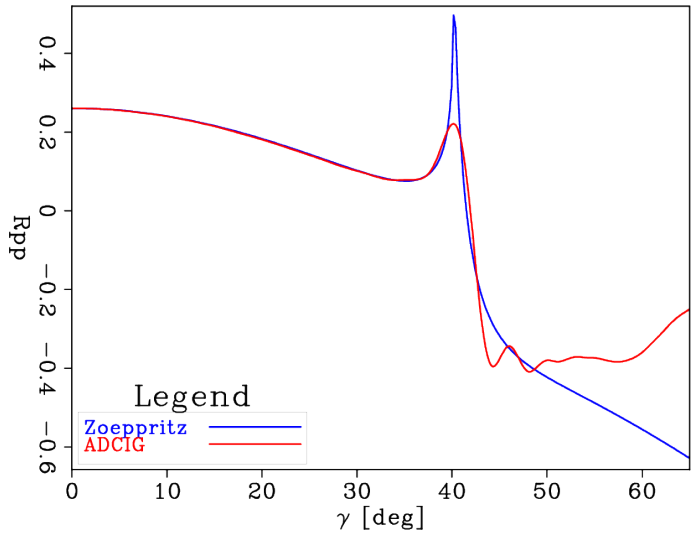

Figure 5: AVA response comparison between the computed PP reflection coefficient (blue curve) and the amplitude variation of the ADCIG extracted at $z = 0.8$ km and $x = 1.7$ km (red curve). [**CR**]

In the second synthetic test, we propagate the elastic wavefield in a subsurface model in which four interfaces are present (Figure 7). In this case, we place 50 sources and 500 receivers at the surface sampled by 50 and 10 meters, respectively. A representative shot gather is shown in Figure 8 in which different events are recorded. Four primary reflections with different AVO behavior can be observed, as well as internal multiples, converted waves, and refracted energy at the farthest offsets.

We perform the extended least-squares migration using the acoustic velocity model shown in Figure 9, which corresponds to the true compressional velocity model but slightly smoothed along the z direction. In this case we apply 500 iterations of linear CG, which corresponds to almost reaching numerical convergence for the regular-

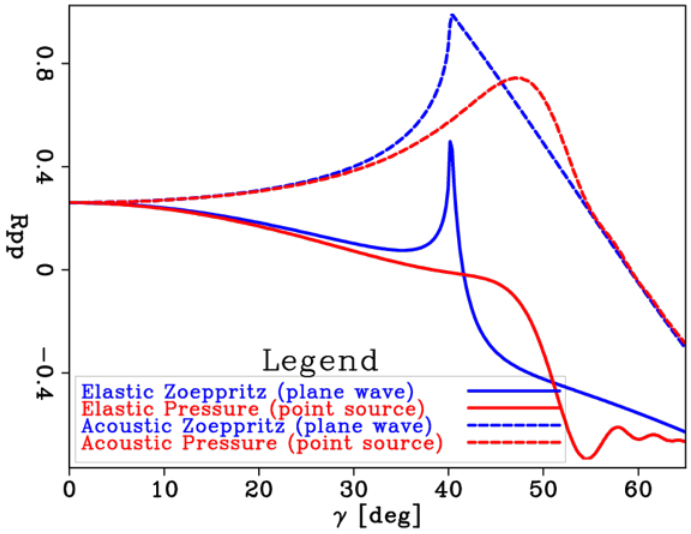

Figure 6: Elastic (solid lines) and acoustic (dashed lines) response comparison for the plane-wave (blue lines) and point-source (red lines) cases. [**CR**]

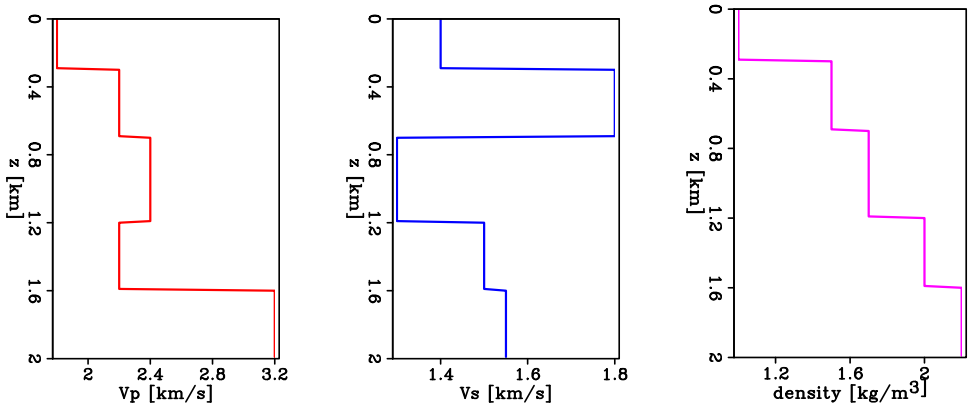

(a) (b) (c)

Figure 7: Elastic parameter profiles of the second synthetic example. [**ER**]

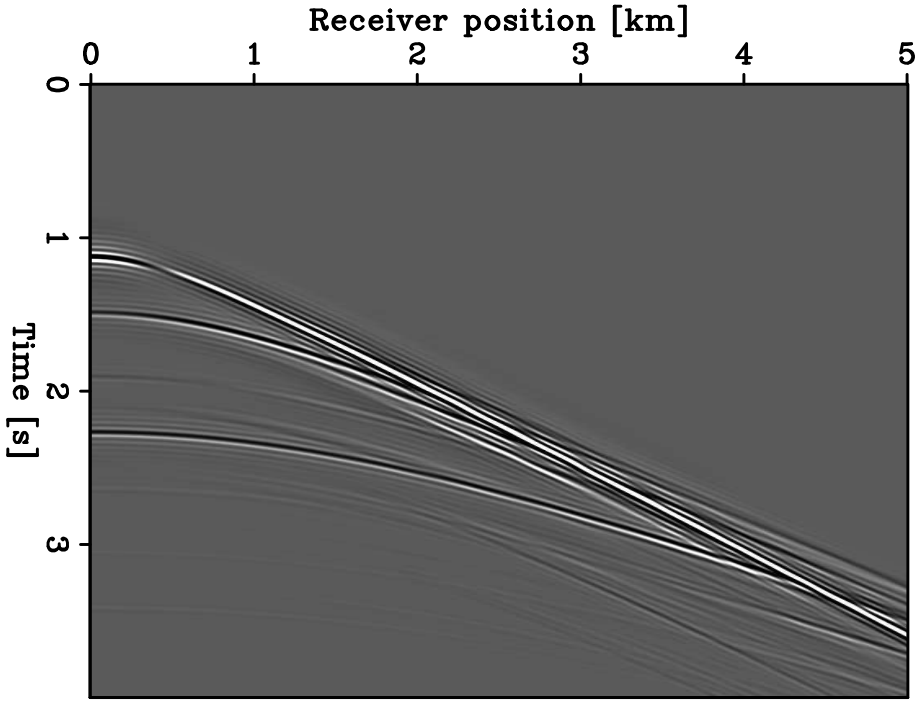

Figure 8: Representative shot gather for the layered model in which the explosive source is placed at the origin. The direct arrival has been removed. [**ER**]

ized problem (i.e., equation 6). The convergence curves of the data-fitting part are shown in Figure 10. The introduction of the regularization term does not allow to entirely match the energy of the recorded data, although the regularized problem almost attains convergence after 500 iterations despite the fact that the non-regularized problem achieves a higher data fit. However, when comparing the ADCIGs extracted at $x = 3.0$ km for the two migration processes (Figure 11), we clearly see better coherence across the angle axis and some suppression of the imaging artifacts when a regularization term is added to the inversion.

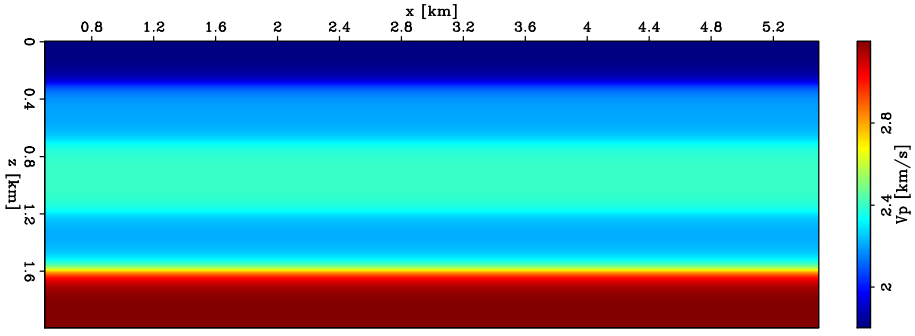

Figure 9: Acoustic migration velocity used within the least- squares RTM process applied to the elastic pressure data recorded over the layered model. [**ER**]

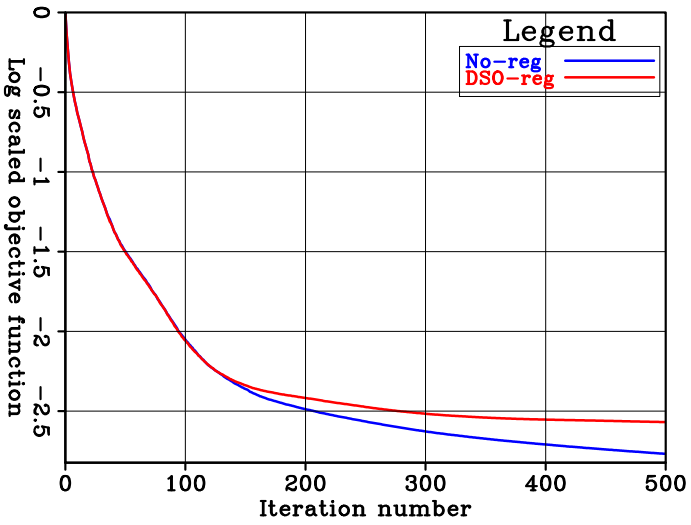

Figure 10: Convergence curves for the non-regularized problem of equation 1 (blue curve) and for the data-fitting term of equation 6 (red curve). [**CR**]

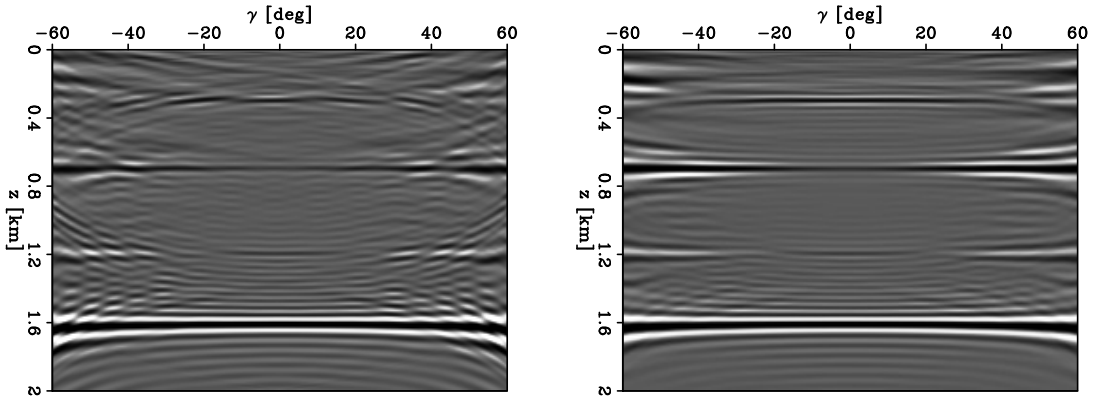

(a) (b)

Figure 11: Comparison between iteratively inverted ADCIGs at $x = 3.0$ km without any regularization (a) and with a DSO regularization term (b). [**CR**]

Figure 12 displays the amplitude response comparison between the theoretical Zoeppritz response and the extracted amplitudes on the ADCIGs of Figure 11 for each interface. Following the previous example, we scaled the responses to obtain an exact match at zero incidence angle. We can clearly see that the amplitude variation of the ADCIGs closely follows the theoretical Zoeppritz response for all the layers. As expected, when a DSO regularization term is used during the inversion, the response becomes smoother and we obtain a better fit with the theoretical one (cf. dashed and solid curves in Figure 12). Despite the fact that we acoustically migrated elastic data that contained energy not present in acoustic primary reflections, the regularized ADCIGs preserve the expected theoretical amplitude behavior as a function of reflection angle.

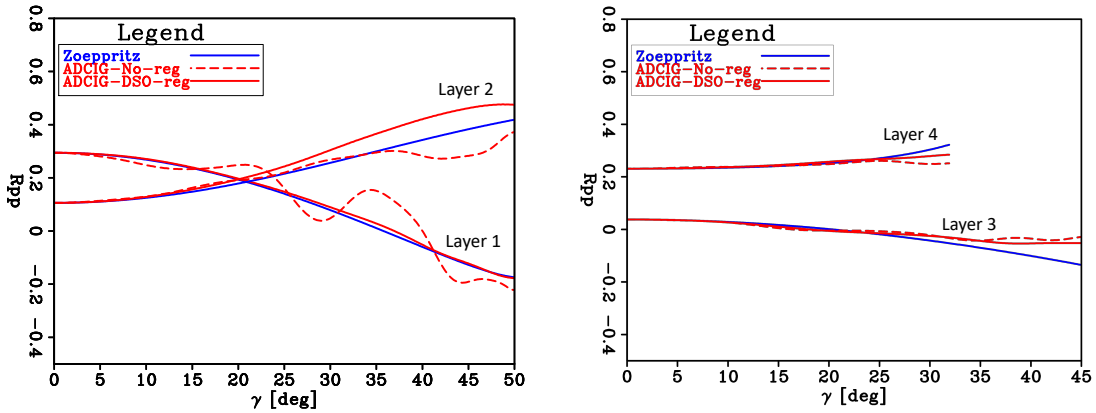

(a) (b)

Figure 12: AVA response comparison for the four-layer model, for the first two layers (a) and for the two deeper ones (b). The blue curves represent the Zoeppritz PP reflection coefficient, while the red ones are the extracted amplitudes from each layer in the ADCIG at $x = 3.0$ km when no regularization is applied (dashed line) and when the DSO operator is employed in the model regularization term (solid line). [**CR**]

CONCLUSIONS

We describe how the extended-image space can be used to construct amplitude-preserving images from elastic pressure data. We make use of the subsurface-offset extension and pose the data migration as a regularized least-squares inverse problem. We then transform the optimal image into the angle domain in which the amplitude behavior can be interpreted via AVA analysis.

In two synthetic tests, we quantitatively demonstrate the ability of the extended space to preserve the correct amplitude response of elastic reflected events. In the first example, we show that the ADCIG fully retains the amplitude response even at and beyond the critical reflection angle. In the second example, we show that the elastic-wave behavior is preserved at each interface, and we demonstrate how

the DSO-regularized approach is able to increase the coherency across angles of the ADCIGs.

ACKNOWLEDGMENTS

We would like to thank Guillaume Barnier for sharing his GPU-based wave-equation library that was employed in this work. Moreover, we thank Chevron Energy Technology Company for permission to publish this work.

REFERENCES

Aki, K., and P. G. Richards, 2002, Quantitative seismology: University Science Books.

Albertin, U., D. Yingst, P. Kitchenside, and V. Tcheverda, 2004, True-amplitude beam migration, *in* SEG Technical Program Expanded Abstracts 2004: Society of Exploration Geophysicists, 949–952.

Aster, R., B. Borchers, and C. Thurber, 2005, Parameter Estimation and Inverse Problems: Elsevier.

Biondi, B., 2003, Amplitude balancing of 3-D angle-domain common-image gathers: SEP-Report, **114**, 45–57.

Biondi, B., and A. Almomin, 2014, Simultaneous inversion of full data bandwidth by tomographic full-waveform inversion: Geophysics, **79**, WA129–WA140.

Biondi, B., and P. Sava, 1999, Wave-equation migration velocity analysis: SEG Technical Program Expanded Abstracts, **18**, 1723–1726.

Gray, S. H., and N. Bleistein, 2009, True-amplitude gaussian-beam migration: Geophysics, **74**, S11–S23.

Kuehl, H., and M. Sacchi, 2002, Robust avp estimation using least-squares wave-equation migration, *in* SEG Technical Program Expanded Abstracts 2002: Society of Exploration Geophysicists, 281–284.

Prucha, M. L., and B. L. Biondi, 2002, Subsalt event regularization with steering filters, *in* SEG Technical Program Expanded Abstracts 2002: Society of Exploration Geophysicists, 1176–1179.

Sava, P. C., and S. Fomel, 2003, Angle-domain common-image gathers by wavefield continuation methods: Geophysics, **68**, 1065–1074.

Schleicher, J., M. Tygel, and P. Hubral, 1993, 3-D true-amplitude finite-offset migration: Geophysics, **58**, 1112–1126.

Shen, P., 2005, Wave equation migration velocity analysis by differential semblance optimization: PhD thesis, Rice University.

Symes, W., and J. J. Carazzone, 1991, Velocity inversion by differential semblance optimization: Geophysics, **56**, 654–663.

Symes, W. W., 2008, Migration velocity analysis and waveform inversion: Geophysical prospecting, **56**, 765–790.

Symes, W. W., and M. Kern, 1994, Inversion of reflection seismograms by differen-

tial semblance analysis: Algorithm structure and synthetic examples: Geophysical Prospecting, **42**, 565–614.

Wang, J., H. Kuehl, and M. D. Sacchi, 2005, High-resolution wave-equation ava imaging: Algorithm and tests with a data set from the western canadian sedimentary basin: Geophysics, **70**, S91–S99.

Yang, T., and P. Sava, 2009, Wave-equation migration velocity analysis using extended images, *in* SEG Technical Program Expanded Abstracts 2009: Society of Exploration Geophysicists, 3715–3719.

Zhang, Y., S. Xu, G. Zhang, and N. Bleistein, 2004, How to obtain true amplitude commonangle gathers from oneway wave equation migration?: SEG Technical Program Expanded Abstracts 2004, Society of Exploration Geophysicists, 1021–1024.

APPENDIX

Equivalence of DSO regularization to smoothing along angles

In this appendix we show the equivalence between minimizing a DSO-regularized ODCIG and a derivative-regularized ADCIG, which mathematically is expressed as follows:

$$\|hI_h(z,h)\|_2^2 \;=\; \left\| \frac{\partial I_\gamma(z,\gamma)}{\partial \gamma} \right\|_2^2, \tag{8}$$

where I_h and I_γ are the ODCIG and ADCIG, respectively. This equivalence has also been proven by Shen (2005).

As shown by Sava and Fomel (2003), the angle-domain transformation is equivalent to a slant-stack operation applied to an ODCIG. If we define $p = -\tan\gamma$, we can write:

$$\begin{aligned} I_\gamma(z,p) &= R_p[I_h(z,h)] = \int I_h(z+ph,h)dh \\ &= \frac{1}{2\pi}\int\int \underline{I_h}(k_z,h)e^{ik_z(z+ph)}dk_z dh \\ &= \frac{1}{2\pi}\int e^{ik_z z}\int \underline{I_h}(k_z,h)e^{ik_z ph}dh dk_z \\ &= \frac{1}{2\pi}\int e^{ik_z z}\underline{I_h}(k_z,k_z p)dk_z, \end{aligned} \tag{9}$$

where the underlined quantities represent Fourier transforms in which we have used known Fourier-domain properties. By using equation 9, we can write the following relation:

$$\begin{aligned} A\{D[I_h(z,h)]\} &= R_p[h\, I_h(z,h)] \\ &= \tfrac{1}{2\pi}\textstyle\int e^{ik_z z}\int h\, \underline{I_h}(k_z,h)e^{ik_z ph}dh dk_z \\ &= -\tfrac{i}{2\pi}\textstyle\int e^{ik_z z}\frac{\partial}{\partial(k_z p)}\underline{I_h}(k_z,k_z p)dk_z \\ &= -i\tfrac{\partial I(z,\gamma)}{\partial\gamma}, \end{aligned} \tag{10}$$

which shows the equivalence in equation 8 when we compute the norm of the last right-hand-side term and assume a unitary angle transform.